FRONTIERS OF PHYSICS

RESEARCH ARTICLE
Volume 21 / Issue 12 / 125206 / 2026

Wigner distribution, Wigner entropy, and quantum refrigerator of a one-dimensional system with off-diagonal and diagonal quasiperiodic modulations

Shan Suo[1,*], Ao Zhou[2,*], Yanting Chen[1], Shujie Cheng[1,2,†], Xianlong Gao[2,‡]

1 Xingzhi College, Zhejiang Normal University, Lanxi 321100, China
2 Department of Physics, Zhejiang Normal University, Jinhua 321004, China
*The authors contribute equally to the work.
Corresponding authors. E-mail: †chengsj@zjnu.edu.cn, ‡gaoxl@zjnu.edu.cn
Received December 29, 2025; accepted April 9, 2026

ABSTRACT

We investigate a one-dimensional system featuring simultaneous off-diagonal and diagonal quasiperiodic modulations. By analyzing the fractal dimension, we map out the delocalization–localization phase diagram. We demonstrate that delocalized and localized states can be distinguished via the Wigner distribution, while extended, critical, and localized phases are separated using the Wigner entropy. Furthermore, we explore the quantum thermodynamic properties, revealing that localized states facilitate the emergence of a quantum heater mode, alongside the appearance of a refrigerator mode. In addition, the efficiency of the quantum engine and the coefficient of performance of the quantum refrigerator are analyzed and discussed. These findings enhance our understanding of localization phenomena and expand the thermodynamic applications of quasiperiodic systems.

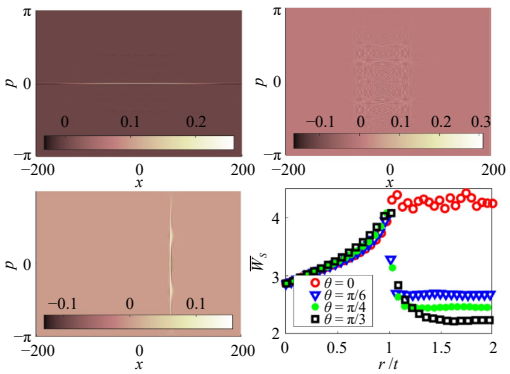

Keywords Anderson localization, Wigner distribution, Wigner entropy, quantum heat engine, quantum refrigerator

1 Introduction

Anderson localization constitutes a fundamental quantum effect in condensed-matter physics, shaping our comprehension of electron dynamics within disordered or quasiperiodic structures [1]. According to scaling theory, three-dimensional systems exhibit a metal–insulator transition that separates an extended phase-allowing free electron propagation-from a localized regime where electronic motion is spatially restricted [2, 3]. Investigations into this phenomenon are essential for deciphering how particles behave in complex disordered environments and for guiding the design and measurement approaches in optical lattice experiments [4–6]. Experimental confirmations of Anderson localization have been achieved across multiple physical setups. For example, ultracold atomic gases offer tunable disorder through precise manipulation of interactions and potentials, enabling direct observation of the transition between delocalized and localized states [6–16]. Similarly, photonic quasicrystals demonstrate localization behavior, with such studies aiding the understanding of light propagation and supporting the creation of advanced optical devices [17–24].

*Special Topic: Non-Hermitian Physics (Editor(s): Peng Xue, Lan Yang & Wu-Ming Liu).

Higher Education Press

https://doi.org/10.15302/frontphys.2026.125206

Depending on the underlying physical mechanisms, Anderson localization manifests in different ways. In quasiperiodic systems, once the quasiperiodic potential surpasses a critical threshold, all quantum states become spatially confined [2]. For quasiperiodic models incorporating short- or long-range hoppings [25–30], shallow modulations [31], as well as generalized quasiperiodic modulations [31–42], localization arises only at certain energy levels; these are separated from delocalized states by mobility edges. This results in an intermediate phase that is neither entirely extended nor fully localized. Recent studies have revealed a hidden self-duality property in certain quasiperiodically modulated systems, deepening theoretical insight into Anderson localization and the formation of mobility edges [43–45].

Despite the established use of inverse participation ratios and fractal dimensions as tools to distinguish quantum phases in quasiperiodic systems, the Wigner distribution [46–52] has emerged as a powerful phase-space framework to differentiate delocalized and localized quantum states [53]. This approach leverages the phase-space representation of quantum states, encoding both position and momentum correlations, which are inaccessible to traditional real-space or momentum-space analyses. The Wigner distribution's inherent ability to capture quantum interference effects — manifested through negative regions in its phase-space density — provides a unique fingerprint for non-classical states, such as those exhibiting Anderson localization or critical behavior. Building on this foundation, the concept of Wigner entropy, defined as the Shannon entropy of the Wigner distribution's magnitude, [54] has been developed to quantify the complexity of mobility edges in phase space [53]. These advances motivate further inquiry into whether Wigner entropy could also help classify different quantum phases, such as extended, critical, and localized phases. Beyond fundamental localization properties, research into quasiperiodic structures has extended to functional applications. Systems featuring mobility edges and intermediate phases, for instance, have been proposed for engineering energy current rectification [55–57] and designing superradiant light sources [58]. Recent work further shows that the extended phase in such systems can support the construction of quantum heat engines [59], whereas the critical phase appears more suitable for implementing quantum heater [59]. Both extended and critical phases also offer advantages for realizing quantum accelerator [59]. This raises an intriguing question: what role might the localized phase play in the development of quantum thermodynamic devices? In addition, quantum thermal cycles employing quasiperiodic systems as the working medium, particularly in the context of quantum refrigerator modes, remain unexplored. If a quasiperiodic system encompassing extended, critical, and localized phases serves as the working medium for a quantum Otto thermal cycle, could a refrigerator mode emerge?

This study explores the localization and thermodynamic properties of one-dimensional off-diagonal quasicrystalline systems, which exhibit both diagonal and off-diagonal quasiperiodic modulation characteristics. By analyzing the fractal dimension, we have constructed a phase diagram that distinguishes between extended, critical, and localized phases. We demonstrate that the Wigner distribution can effectively distinguish between delocalized and localized states, while the Wigner entropy (which is maximum in the critical phase, intermediate in the extended phase, and minimum in the localized phase) serves as a reliable tool for classifying these quantum phases. Furthermore, when the system is used as a working medium in a quantum non-adiabatic cycle, we find that the extended phase supports a quantum heat engine mode, while the localized phase tends more towards a heater mode; whereas when the system is used as a working medium in a quantum Otto cycle, a refrigerator mode emerges. These findings enhance our understanding of the phase space approach in quasiperiodic systems and highlight its potential in thermodynamic applications.

This work is organized as follows. Section 2 studies the off-diagonal quasicrystal with both diagonal and off-diagonal modulations and gives out the localization phase diagram by the fractal dimension. Section 3 studies Wigner distributions and the Wigner entropy. Section 4 studies the thermodynamical applications of the quantum non-adiabatic and adiabatic Otto cycle and analyze the efficiency of quantum heat engine and the coefficient of performance of the quantum refrigerator. A summary is presented in Section 5.

2 Model and localization phase diagram

A one-dimensional system with both off-diagonal and diagonal quasiperiodic modulations is studied, and its Hamiltonian is given by

$$H = \sum_n \left(t_n \hat{c}_n^\dagger \hat{c}_{n+1} + H.c.\right) + \sum_n V_n \hat{c}_n^\dagger \hat{c}_n, \tag{1}$$

where $t_n = t + t_1 \cos(2\pi\alpha n)$ and $V_n = V\cos(2\pi\alpha n)$. t is the unit of energy. t_1 and V are tunable hopping parameter and potential amplitude, respectively. $\alpha = \frac{\sqrt{5}-1}{2}$ is the incommensurate number which leads to the term 'quasiperiodic modulation'.

The inverse participation ratio (IPR) is a commonly used tool for determining the localization and delocalization properties of wave functions of a system. For a normalized wave function $\psi_j = \sum_{n=1}^{L} \phi_j(n)\hat{c}_n^\dagger|0\rangle$, where j is the index of the energy level which is arranged in ascending order, the associated IPR_j is given by

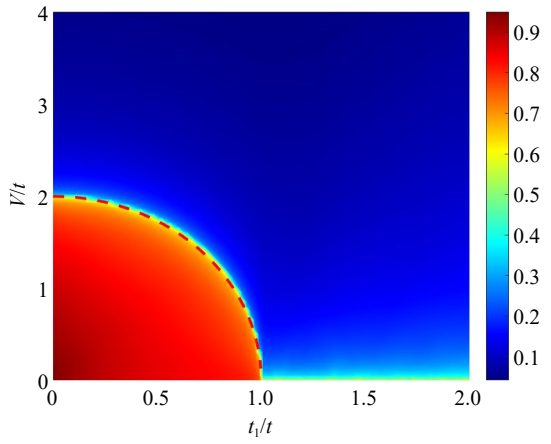

Fig. 1 The phase diagram shows how fraction dimension D changes with the ratios V/t and t_1/t. The color corresponds to the numerical values of D. The red dashed line denotes the phase boundary, which serves to separates the extended phase ($D \sim 1$) from the localized ($D \sim 0$) and critical phase ($D \sim 0.5$). The involved parameter is $L = 2584$.

$$\mathrm{IPR}_j = \sum_{n=1}^{L} |\phi_j(n)|^4. \tag{2}$$

For the extended states, critical states, and localized states, their corresponding IPR respectively have the following characteristics: $\mathrm{IPR} \to \frac{1}{L}$ (which tends to zero under large system size), $0 < \mathrm{IPR} < 1$, and $\mathrm{IPR} \to 1$ [27, 60]. By averaging the IPR of all energy levels, we can obtain the mean inverse participation ratio (MIPR), which is defined as $\mathrm{MIPR} = \sum_{j=1}^{L} \mathrm{IPR}_j/L$. With MIPR, we can distinguish among extended phase, critical phase and localized phase. In the following, we will employ the scaling index of MIPR, i.e., the fractal dimension [61–63] D to characterize the potential quantum phases of the system, and it is defined as $D = -\frac{\ln \mathrm{MIPR}}{\ln L}$. According to the characteristics of inverse participation ratio, the corresponding MIPR of extended phase also scales as $1/L$, so the corresponding fractal dimension D tends to 1. The MIPR of the critical phase is still within the interval $(0, 1)$, so the D corresponding to the critical phase is within $(0, 1)$. The MIPR corresponding to the localized phase tends to 1, so the D corresponding to the localized phase tends to 0.

Choosing the system size $L = 2584$, the phase diagram illustrating the fractal dimension D in V–t_1 parameter space is plotted in Fig. 1, in which the color represents the fractal dimension D. In fact, the earlier studies have established that the system undergoes a phase transition between the extended phase and the critical phase for the $V = 0$ case [64]. It can be observed from Fig. 1(a) that at $V = 0$, the fractal dimension D corresponding to the extended phase approaches 1, whereas the D value associated with the critical phase converges to 0.5. Drawing on this finding, we may deduce that under the condition of finite V, the quarter-elliptic region where D is close to 1 corresponds to the extended phase. In contrast, the area outside this region exhibits a D value that tends toward 0, which indicates that it belongs to the localized phase.

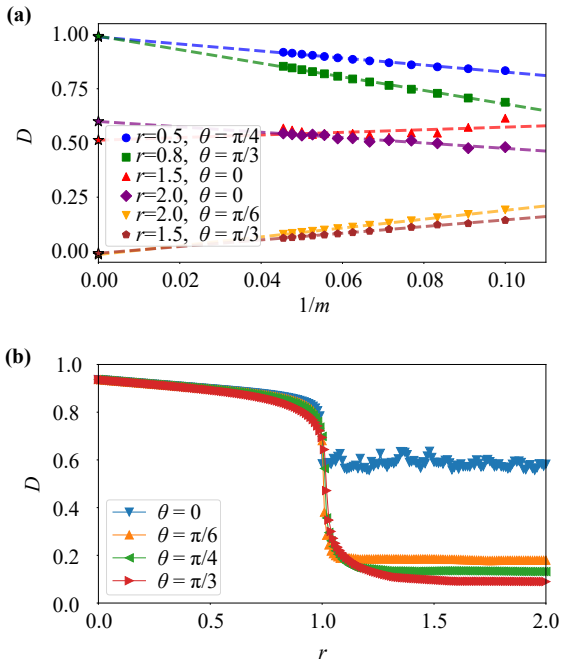

Fig. 2 **(a)** Fractal dimension D as functions of r under $\theta = 0$, $\pi/4$, $\pi/3$, and $\pi/6$. **(b)** Finite size analysis of D under different (r, θ), with $1/m$ the inverse Fibonacci index.

In contrast to the non-Hermitian case [65], the restoration of the system's Hermiticity enlarges the region of the extended phase. To identify the phase boundary of the extended-localized transition, we introduce the transformation $r = \sqrt{\frac{V^2}{4} + t_1^2}$ where $\theta = \arctan(V/t_1) \in [0, 2\pi]$. For the system with $L = 610$, the plots of D against r under various θ values are presented in Fig. 2(a). It is intuitively observable that for all distinct θ, the D–r curves that characterize the extended-localized (critical) transition all exhibit an abrupt jump at the critical value $r_c/t = 1$. This critical condition corresponds to the phase boundary $\sqrt{\frac{V^2}{4} + t_1^2} = t$, which is depicted as the red dashed line in Fig. 1.

To further verify the above mentioned conclusions we have drawn, we perform the finite size analysis on D. We consider a system where the system size L equals the m-th Fibonacci number F_m and the incommensurate parameter α is replaced by $\alpha = F_{m-1}/F_m$. In the limit of $1/m \to 0$ (extrapolation limit), $D \to 0$ indicates a localized state, $0 < D < 1$ points to a critical state, and $D \to 1$ signifies an extended state. We choose representative parameter points in various phases to compute D. As depicted in Fig. 2(b), we observe that the relevant D approaches 1 at the parameter sites $(r, \theta) = (0.5t, \frac{\pi}{4})$ and

$(r,\theta)=\left(0.8t,\frac{\pi}{3}\right)$. This observations confirm that the system resides in the extended phase under these conditions. As anticipated, the corresponding D values fall within the interval $(0,1)$ in the thermodynamic limit when $(r,\theta)=(1.5t,0)$ and $(r,\theta)=(2t,0)$. These results clearly reveal the system's critical-phase characteristics in such parameter regimes. When $(r,\theta)=\left(1.5t,\frac{\pi}{3}\right)$ and $(r,\theta)=\left(2t,\frac{\pi}{6}\right)$, the associated D extrapolates to 0. This outcome identifies that the system is in the localized phase at these parameter points.

3 Wigner distribution and Wigner entropy

A recent investigation [53] revealed that the quantum phase space representation, specifically the Wigner distribution, is capable of distinguishing among the extended state, the critical state, and the localized state. Building on the Wigner distribution, the Wigner entropy can be further derived; subsequent findings indicate that the Wigner entropy of critical states is the largest, that of extended states falls in the middle range, and that of localized states is the smallest. Leveraging this characteristic, the mobility edge can also be identified. These findings offer valuable insights for our subsequent research into whether the Wigner entropy can be employed to discriminate among the extended phase, the critical phase, and the localized phase.

For a given wave function $|\psi\rangle$, the Wigner distribution function $W(x,p)$ can be derived via the integral expression presented below [46–52]:

$$W(x,p)=\frac{1}{2\pi\hbar}\int_{-\infty}^{\infty}\left\langle x-\frac{y}{2}\right|\hat{\rho}\left|x+\frac{y}{2}\right\rangle \mathrm{e}^{-\frac{\mathrm{i}py}{\hbar}}\,\mathrm{d}y, \tag{3}$$

where x and p represent the coordinate and momentum in phase space, respectively; $\hbar$ denotes the reduced Planck constant, and $\hat{\rho}=|\psi\rangle\langle\psi|$ is the density matrix. The Wigner distribution function can simultaneously describe the position and momentum information of particles, and it is a quasi-probability distribution function. Building on the Wigner distribution, the Wigner entropy (denoted as W_S) can be further derived [54]. Taking into account the negativity of $W(x,p)$, the final calculation of W_S adopts the following definition:

$$W_S=-\iint W(x,p)\ln|W(x,p)|\mathrm{d}x\mathrm{d}p, \tag{4}$$

where the integral range for x is $[-L/2,L/2]$, and the corresponding integral interval for p is $[-\pi,\pi]$.

In principle, the localized, critical, and extended properties of wave functions can be better distinguished for larger system sizes. For the Wigner distribution, however, these three quantum states can be well distinguished even with a smaller system size [53]. In addition, the smaller system size can save the cost of computing time. We follow the strategy outlined in Ref. [53], taking

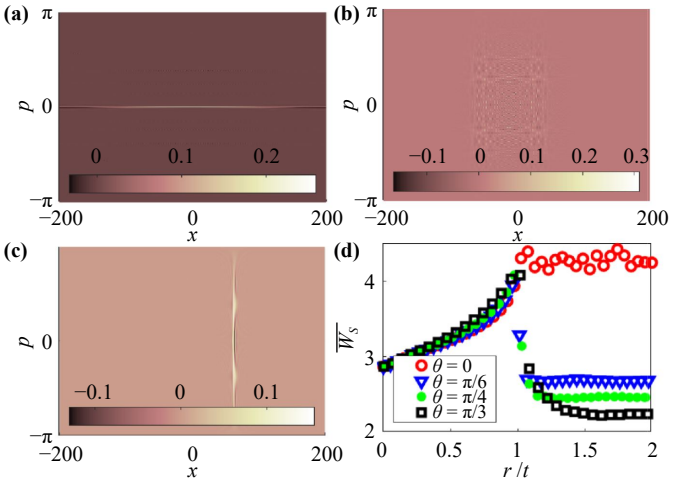

Fig. 3 **(a)** Wigner distribution $W(x,p)$ of an extended state under $r=0.5t$ and $\theta=\frac{\pi}{4}$. **(b)** Wigner distribution $W(x,p)$ of a critical state under $r=1.5t$ and $\theta=0$. **(c)** Wigner distribution $W(x,p)$ of a localized state under $r=2t$ and $\theta=\frac{\pi}{6}$. **(d)** The mean Wigner entropy $\overline{W}_S$ as a function of r under various θ. Other involved parameter is $L=400$.

a relatively small system size $L=400$, the Wigner distribution $W(x,p)$ of a typical extended state is depicted in Fig. 3(a), that of a typical critical state is presented in Fig. 3(b), and the Wigner distribution corresponding to a typical localized state is plotted in Fig. 3(c). Here, the typical states are the ground states. It can be observed that the $W(x,p)$ of the extended state remains extended along the x branch, while it is relatively concentrated in the p direction, primarily localized around $p=0$. We briefly explain why the Wigner distribution $W(x,p)$ for extended states is concentrated mainly at $p=0$. At first, the system possesses time-reversal symmetry, which endows the wave function with complex conjugation symmetry, namely $\phi^*(x)=\phi(x)$. From the Fourier transformation, the momentum-space wave function satisfies even conjugation symmetry, i.e., $\phi^*(p)=\phi(-p)$, which directly leads to an even-symmetric probability distribution in momentum space, $|\phi(p)|^2=|\phi(-p)|^2$. Integrating $W(x,p)$ over the coordinate x yields the momentum-space probability density, $\int W(x,p)\mathrm{d}x=|\phi(p)|^2$, whose even symmetry directly reflects that $W(x,p)$ is symmetric about $p=0$. Furthermore, for extended states, the $W(x,p)$ in the x branch is distributed across the entire system, the position uncertainty Δx is maximized. According to the Heisenberg uncertainty relation $\Delta x\Delta p\geq\frac{\hbar}{2}$, the p branch should have a minimal momentum uncertainty Δp, therefore, $W(x,p)$ for extended states is concentrated mainly at $p=0$.

For the critical state, the $W(x,p)$ exists on both the x branch and p branch, exhibiting a certain level of broadening. In contrast, the $W(x,p)$ of the localized state remains localized along the x branch yet appears

extended along the p branch. These features can be understood by the Heisenberg uncertainty relation as well. Under the condition of constant error, the distribution of the wave function in the critical state is sub-extended. Its position uncertainty is smaller than that of the extended state, but its momentum uncertainty is relatively larger than that of the extended state. This means that the Wigner distribution $W(x,p)$ of the critical state presents a sub-extended distribution state on both the x and p branches. The wave function distribution of the localized state is highly concentrated, and its position uncertainty is the smallest among the three states, so its momentum uncertainty is the largest among these three states. Therefore, it can be understood that the $W(x,p)$ of the localized state is localized on the x branch and extended on the p branch. For a wave function, we can obtain the Wigner entropy corresponding to different wave functions by statistically analyzing the Wigner distribution, thereby distinguishing different wave functions. It should be noted that for a quantum phase, the characteristics of the wave functions corresponding to all energy levels and the Wigner distribution are similar. Thus, we can utilize the physical quantity that characterizes the common features of the wave function and the Wigner distribution, namely the mean Wigner entropy $\overline{W}_S$, i.e., $\overline{W}_S = \sum_{j=1}^{L} W_s^j$, to represent different quantum phases, thereby characterizing the Anderson localization phase transition. Considering different θ values, the variation curves of the mean Wigner entropy $\overline{W}_S$ with respect to r are shown in Fig. 3(d). It can be observed that the $\overline{W}_S$ undergoes a jump at $r = t$. The $\overline{W}_S$ of the critical phase is the largest, followed by the extended phase, and the localized phase is the smallest. These findings support the fact that Wigner entropy can not only distinguish wave functions with different properties, but also quantum phases with different properties.

4 Thermodynamical applications

Recently, it has been revealed that quasiperiodic systems have rich thermodynamic applications, such as quantum heat engine, quantum heater and quantum accelerator. In particular, it has been proven that the extended phase serves to sustain the working mode of quantum heat engine, while the critical phase is beneficial for maintaining the working modes of quantum heater [59]. In the present section, we focus on exploring the thermodynamic applications of this generalized Aubry–André (AA) model incorporating both diagonal and off-diagonal quasiperiodic modulations. Our core objectives are to verify whether the extended phase of this model still contributes to preserving the working mode of quantum heat engine, and to clarify which specific working mode the localized phase tends to favor, as well as to explore whether there exists a fourth thermodynamic working mode, namely the quantum refrigerator.

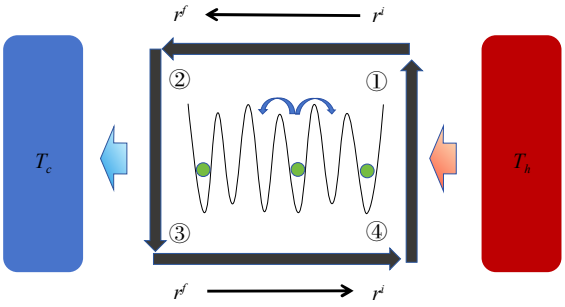

Fig. 4 Schematic illustration of the four-stroke quantum non-adiabatic heat cycle process. T_h and T_c stand for the high-temperature and low-temperature heat sources, respectively. The working medium employed is the generalized AA model with diagonal and off-diagonal quasiperiodic modulations. r^i and r^f represent the systematic parameters of the corresponding Hamiltonians. The system size is $L = 610$.

Compared to the quantum Otto cycle analyzed later, its lattice site occupation probability during heat exchange and thermal equilibrium satisfies the canonical ensemble, and the lattice site occupation probability during expansion and compression is influenced by the instantaneous wave function. Therefore, this cycle can significantly reflect the influence of localization effects. This is why we specifically included it in our study. The first (④ → ①) and third (② → ③) strokes take place under thermal contact with high-temperature (T_c) heat baths. These strokes proceed in the absence of external driving forces or particle exchange. From a thermodynamic perspective, the second (① → ②) and fourth (③ → ④) strokes are isolated from the thermal sources. However, they may not be strictly adiabatic in the quantum-mechanical sense, as quantum transitions can arise during the practical evolutionary process. After the working medium undergoes this complete cycle, we can determine the heat absorbed Q_h ($Q_h = E_1 - E_4$) from the T_h source, the heat released Q_c ($Q_c = E_3 - E_2$) to the T_c source, and the net work W done by the working medium, where $W = Q_h + Q_c$. Here, E_1, E_2, E_3, and E_4 are the energies of the four stages, i.e., ①, ②, ③, and ④, respectively. Notably, the heat cycle process complies with the Clausius inequality, which serves as a fundamental cornerstone of thermodynamics. Based on the specific values of Q_h, Q_c, and W, the engine that employs the extended-localized (critical) quasiperiodic system as its working medium demonstrates distinct operational modes [66, 67]:

1) Heat engine: $Q_h > 0$, $Q_c < 0$, and $W > 0$;
2) Refrigerator: $Q_h < 0$, $Q_c > 0$, and $W < 0$;
3) Heater: $Q_h < 0$, $Q_c < 0$, and $W < 0$;
4) Accelerator: $Q_h > 0$, $Q_c < 0$, and $W < 0$.

In the first stroke, the working medium, which is characterized by the Hamiltonian $H(r^i)$, will ultimately

attain thermal equilibrium and relax into a Gibbs state. The density matrix ρ_1 of this state is expressed as $\rho_1 = \frac{e^{-\beta_h H(r^i)}}{Z_1}$, where $\beta_h = \frac{1}{k_B T_h}$ (k_B denotes the Boltzmann constant) and $Z_1 = \mathrm{Tr}\left[e^{-\beta_h H(r^i)}\right]$ represents the partition function. Therefore, at thermal equilibrium, the system energy is given by $E_1 = \mathrm{Tr}\left[\rho_1 H(r^i)\right]$. In the third stroke, the medium with $r = r^f$ is brought into contact with a heat source featuring $\beta_c = \frac{1}{k_B T_c}$. Consequently, the corresponding Gibbs state is $\rho_3 = \frac{e^{-\beta_c H(r^f)}}{Z_2}$, with the partition function defined as $Z_2 = \mathrm{Tr}\left[e^{-\beta_c H(r^f)}\right]$. The energy of the medium at this stage is then $E_3 = \mathrm{Tr}\left[\rho_3 H(r^f)\right]$.

For the second and fourth strokes, we first consider the non-adiabatic scenario, where the density matrix remains approximately unchanged throughout the evolutionary process. This idea can be realized in the future by making use of the continuously developing quantum feedback technology [68–73]. During the second stroke, the Hamiltonian parameter is switched from r^i to r^f. In this stroke, heat exchange and work exchange occur simultaneously. The Gibbs state ρ_2 in this stroke remains approximately unaltered, i.e., $\rho_2 \approx \rho_1$, we adopt $\rho_2 = \rho_1$ in actual analysis, while the energy E_2 is updated to $E_2 = \mathrm{Tr}\left[\rho_2 H(r^f)\right]$. The fourth stroke can be interpreted as a thermal annealing process. In this process, the hopping parameter of the medium is switched back from r^f to r^i; however, the Gibbs state ρ_4 remains approximately equal to ρ_3 ($\rho_4 \approx \rho_3$) and we adopt $\rho_4 = \rho_3$ in actual analysis. Thus, the energy of the medium becomes $E_4 = \mathrm{Tr}\left[\rho_4 H(r^i)\right]$.

For a system with size $L = 610$ and $k_B T_c = 0.1t$, after analyzing the values of Q_h, Q_c and W, the corresponding working modes of the four-stroke cycle under different r^f and θ are plotted in Figs. 5(a)–(f), respectively. It can be observed that this cycle exhibits a diverse range of working modes. The brown regions represent the *Heat engine* mode. The yellow regions correspond to the *Accelerator* mode, while the green regions indicate the *Heater* working mode. It is noted from Figs. 5(a)–(d) that when r^f and r^i are below the critical value r_c, the *Heat engine* mode appears. This suggests that similar to the results of the critical-extended quasiperiodic system [59], for the quasiperiodic system under a finite V, its extended phase is favorable for the design of a quantum heat engine as well. As r^f increases and surpasses the critical values $r_c = t$, the system enters the localized phase. From Figs. 5(e) and (f), we can see that regions representing the *Heater* mode expand. This indicates that the localized phase is more conducive to the realization of a quantum heater. Additionally, it is clear that there are extensive parameter ranges corresponding to the *Accelerator* mode, regardless of whether the system is in the extended phase or the localized phase. Combining with previous research on extended-critical quasiperiodic system [59], we draw a conclusion that all the extended, critical and localized phases facilitate the realization of a quantum accelerator, and both the localized and critical phases are conducive to the realization of quantum heater.

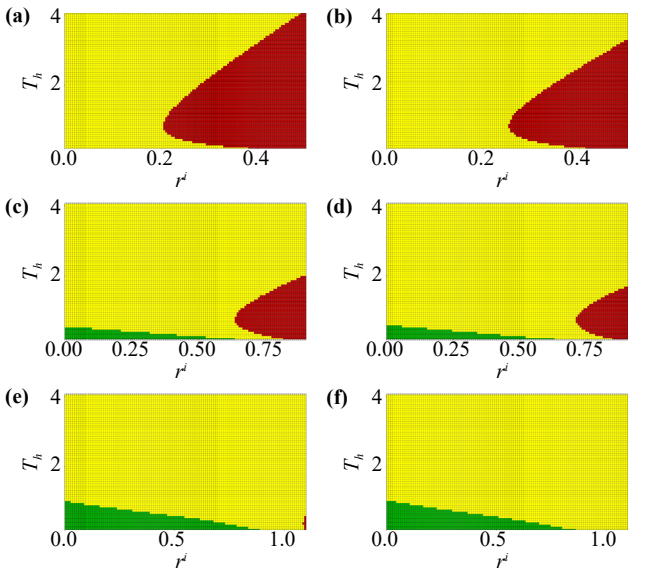

Fig. 5 Working modes of the four-stroke cycle in the non-adiabatic case. **(a)** $r^f = 0.5t$ and $\theta = \pi/6$. **(b)** $r^f = 0.5t$ and $\theta = \pi/4$. **(c)** $r^f = 0.9t$ and $\theta = \pi/6$. **(d)** $r^f = 0.9t$ and $\theta = \pi/4$. **(e)** $r^f = 1.1t$ and $\theta = \pi/6$. **(f)** $r^f = 1.1t$ and $\theta = \pi/4$. The brown regions (■) represent the *Heat engine*. The yellow regions (■) denote the *Accelerator* and the green regions (■) denote the *Heater*. Other parameters are $L = 610$, $k_B = 1$ and $T_c = 0.1t$.

Moreover, the results shown in Fig. 5 offer strategies for regulating the working mode of the four-stroke cycle. The transition between different working modes can be achieved by tuning r^f, r^i, and $k_B T_h$. For example, when r^f is much smaller than r_c [see Figs. 5(a) and (b)], there are two working modes. Within a certain range of $k_B T_h$, increasing r^i can switch the system's working mode between *Accelerator* and *Heat engine*, or vice versa. When r^f is close to but still less than r^c and $k_B T_h$ is small [refer to Figs. 5(c) and (d)], there are three working modes. Thus, the cycle's working mode will change from *Heater* to *Accelerator* and then to *Heat engine* when we gradually increase r^i. When r^f is larger than r_c, the cycle can be toggled between *Heater* and *Accelerator* modes by tuning r^i or $k_B T_h$.

Figure 6 depicts the variation of the efficiency η of a non-adiabatic heat engine with T_h and r^i under different values of r^f and θ. The definition of η reads

$$\eta = \frac{W}{Q_h} = \frac{Q_c + Q_h}{Q_h}. \tag{5}$$

The results on the left and right panels of Fig. 6 are obtained at $\theta = \pi/6$ and $\theta = \pi/4$ respectively. It can be seen that the efficiency distribution has a common feature: the efficiency is the highest when T_h is relatively

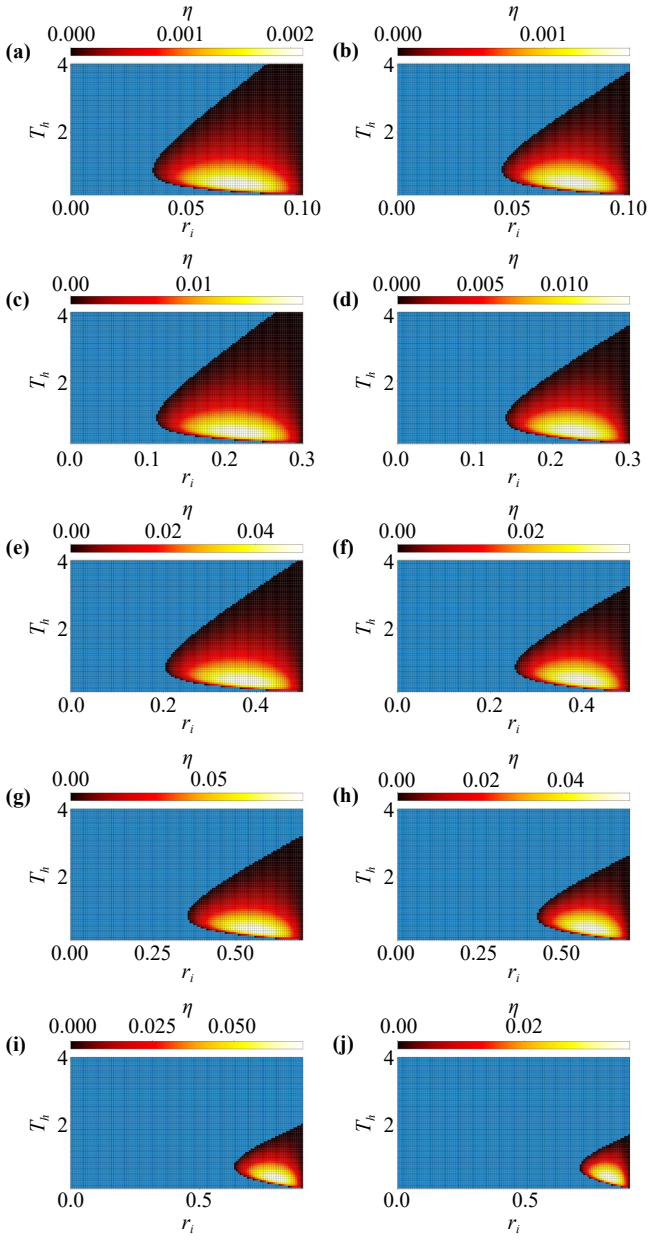

Fig. 6 Efficiency of the heat engine mode in the non-adiabatic case. **(a)** $r^f = 0.1t$ and $\theta = \pi/6$. **(b)** $r^f = 0.1t$ and $\theta = \pi/4$. **(c)** $r^f = 0.3t$ and $\theta = \pi/6$. **(d)** $r^f = 0.3t$ and $\theta = \pi/4$. **(e)** $r^f = 0.5t$ and $\theta = \pi/6$. **(f)** $r^f = 0.5t$ and $\theta = \pi/4$. **(g)** $r^f = 0.7t$ and $\theta = \pi/6$. **(h)** $r^f = 0.7t$ and $\theta = \pi/4$. **(i)** $r^f = 0.9t$ and $\theta = \pi/6$. **(j)** $r^f = 0.9t$ and $\theta = \pi/4$. The color of the color bar corresponds to the efficiency value, while the blue part indicates the non-heat engine part. Other parameters are $L = 610$, $k_B = 1$ and $T_c = 0.1t$.

low and r_i is close to r_f. However, it cannot be denied that the efficiency of quantum heat engines still has a certain gap compared with the Carnot efficiency η_C ($\eta_C = 1 - T_c/T_h$). Besides, we can observe that the efficiency variation exhibits anisotropic characteristics: under the same value of r^f, the peak efficiency at $\theta = \pi/6$ is slightly higher than that at $\theta = \pi/4$. When $\theta = \pi/6$, it can be seen that the peak efficiency shows a gradually increasing trend. However, in the case of $\theta = \pi/4$, it can be seen that the peak efficiency firstly decreases and then increases.

Next, we study the adiabatic process. The calculation steps for energy E_1 in the first stroke and energy E_3 in the third stroke are almost consistent with those in the non-adiabatic case, the only difference lies in the fact that when the working substance exchanges heat with a large heat source and reaches thermal equilibrium, the system satisfies the grand canonical ensemble statistics, and the chemical potential has been set to 0. In the second stroke, we assume that the system evolves from the r^i state to the r^f state in the quantum adiabatic form. Therefore, the occupation probability of the particles remains unchanged. By using the method of statistical mechanics, the partition function Z_2 is derived as $Z_2 = \prod_{j=1}^{L}\left(e^{-\beta_2 E_j^i}\right)$, where $\beta_2 = \frac{1}{k_B T_h}$, and E_j^i denotes j-th energy level of the working medium in the r^i state. Further, the energy E_2 is obtained as $E_2 = \sum_{j=1}^{L} E_j^f f(E_j^i)$, where E_j^f denotes the j-th energy level of the working medium in the r^f state and $f(E_j^i) = \frac{1}{1+e^{\beta_2 E_j^i}}$ represents the Fermi-Dirac distribution function. Similarly, in the fourth stroke, we assume that the system also evolves from the r^f state to the r^i state in the form of quantum adiabatic. Thus, during the evolutionary process, the occupation probability of particles at each energy level remains unchanged. By using the method of statistical physics, the partition function $Z_4 = \prod_{j=1}^{L}\left(e^{-\beta_4 E_j^f}\right)$, where $\beta_4 = \frac{1}{k_B T_c}$, is obtained. Further, we obtain the energy E_4 as $E_4 = \sum_{j=1}^{L} E_j^i f(E_j^f)$, where $f(E_j^f) = \frac{1}{1+e^{\beta_4 E_j^f}}$ is the Fermi–Dirac distribution function.

Still taking system size $L = 610$ and $k_B T_c = 0.1t$, the working modes of four-stroke cycles under different r^f and θ are shown in Figs. 7(a)–(d). It is readily seen that similar to the non-adiabatic case, the *Accelerator* mode occupies the vast majority of the parameter space and is almost independent of the selection of r^f and θ, indicating that the *Accelerator* mode does not depend on the properties of the system. The left working modes show obvious parameter dependencies. It can be seen from Figs. 7(a) and (b) that the *Heat engine* mode only exists in the extended phase regime. However, compared with the non-adiabatic case, the *Heat engine* mode in the adiabatic case is more sensitive to changes in the parameter r^f. As can be seen from Figs. 7(a)–(d), when r^f is slightly increased, the *heat engine* mode disappears. Moreover, it can be seen that the adiabatic condition compresses the high-temperature threshold of the *Heat engine* mode, making the *Heat engine* in the adiabatic condition only operate at a lower heat source temperature. As can be seen from Figs. 7(e) and (f), as the working medium in contact with the low-temperature heat source enters the scope of the localized phase, the

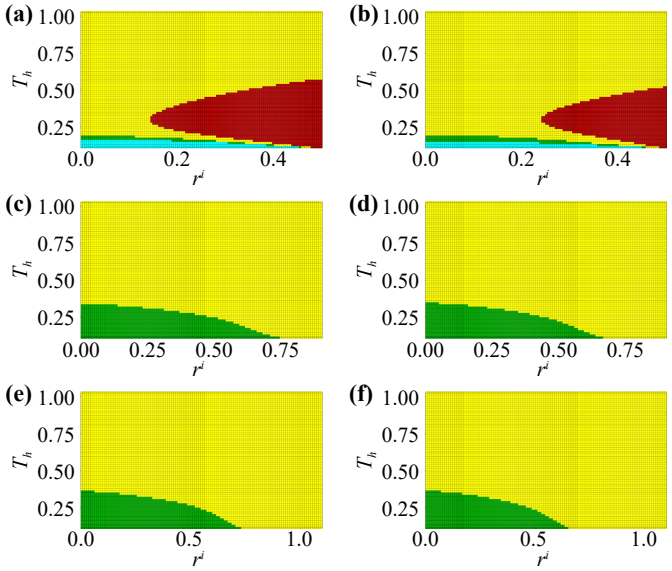

Fig. 7 Working modes of the four-stroke cycle in the adiabatic case. **(a)** $r^f = 0.5t$ and $\theta = \pi/6$. **(b)** $r^f = 0.5t$ and $\theta = \pi/4$. **(c)** $r^f = 0.9t$ and $\theta = \pi/6$. **(d)** $r^f = 0.9t$ and $\theta = \pi/4$. **(e)** $r^f = 1.1t$ and $\theta = \pi/6$. **(f)** $r^f = 1.1t$ and $\theta = \pi/4$. The brown regions (■) represent the *Heat engine*. The blue regions (■) represent the *Refrigerator*. The yellow regions (■) denote the *Accelerator* and the green regions (■) denote the *Heater*. Other parameters are $L = 610$, $k_B = 1$ and $T_c = 0.1t$.

working area of the *Heater* mode increases, indicating that the localized phase is conducive to the existence of the *Heater* mode. However, compared with the non-adiabatic case, the working area slightly decreases. Surprisingly, after taking into account the adiabatic process, the *Refrigerator* mode emerges in the extended phase regime, as shown in the green areas in Figs. 7(a) and (b). However, the *Refrigerator* is also parameter-sensitive. As r^f increases, the *Refrigerator* mode disappears. Moreover, a higher heat source temperature is also not conducive to the emergence of the *Refrigerator*. But at least, these findings indicates that the adiabatic evolution process and appropriate parameter settings can trigger the *Refrigerator* mode.

To analyze the efficiency of the quantum Otto heat engine in the adiabatic case, we select the same parameters as those used in Fig. 6. The results of η of the heat engine mode are plotted in Figs. 8(a)–(h). Similar to the previous non-adiabatic case, the peak efficiency of the heat engine in the adiabatic case still has a certain gap from η_C. Furthermore, as in the non-adiabatic case, the high efficiency of the heat engine in the adiabatic case also occurs at relatively small T_h. Moreover, for relatively large r^f, the peak efficiency is also attained when r^i is close to r^f. A notable difference, however, is that for relatively small r^f, the distribution of high efficiency in the adiabatic case is broader. Similarly, the efficiency variation under adiabatic conditions remains anisotropic, consistent with the non-adiabatic situation. The distinction

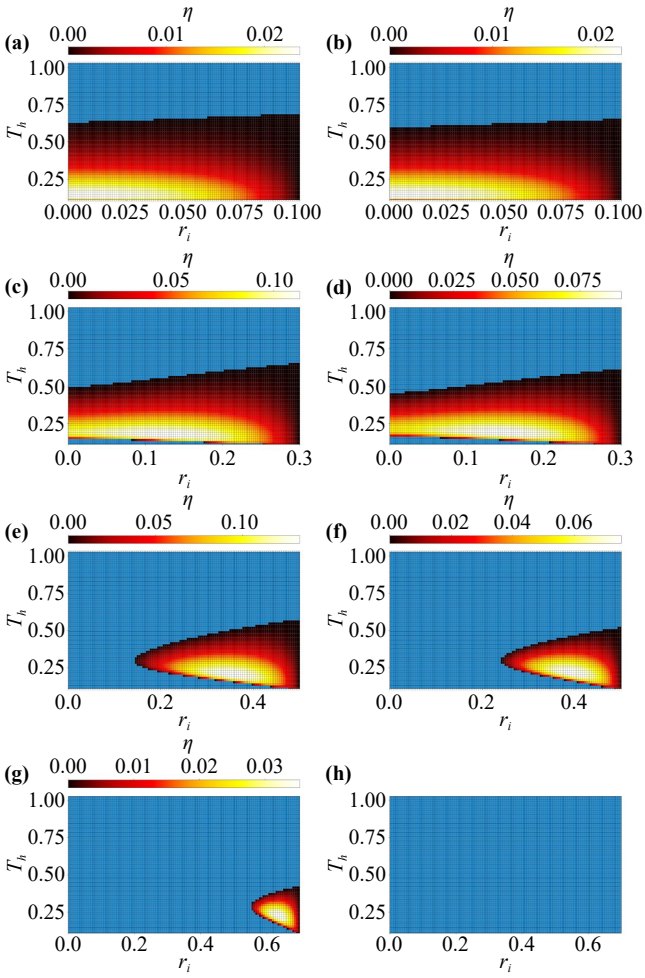

Fig. 8 Efficiency η of the heat engine mode in the adiabatic case. **(a)** $r^f = 0.1t$ and $\theta = \pi/6$. **(b)** $r^f = 0.1t$ and $\theta = \pi/4$. **(c)** $r^f = 0.3t$ and $\theta = \pi/6$. **(d)** $r^f = 0.3t$ and $\theta = \pi/4$. **(e)** $r^f = 0.5t$ and $\theta = \pi/6$. **(f)** $r^f = 0.5t$ and $\theta = \pi/4$. **(g)** $r^f = 0.7t$ and $\theta = \pi/6$. **(h)** $r^f = 0.7t$ and $\theta = \pi/4$. The color of the color bar corresponds to the efficiency value, while the blue part indicates here is not a heat engine mode. Other parameters are $L = 610$, $k_B = 1$ and $T_c = 0.1t$.

lies in the trend of peak efficiency with angle: at $\theta = \pi/6$, the adiabatic peak efficiency first rises and then falls, whereas at $\theta = \pi/4$ it exhibits a gradual decline.

In the following, we analyze the coefficient of performance (COP) of the refrigerator mode, and the COP is defined as

$$\mathrm{COP} = \frac{Q_c}{W}. \tag{6}$$

Conventional wisdom suggests that the performance of a refrigerator should not exceed the Carnot coefficient of performance (denoted by $\mathrm{COP_C}$) corresponding to the ideal Carnot refrigerator cycle, which is given by

$$\mathrm{COP_C} = \frac{T_c}{T_h - T_c}. \tag{7}$$

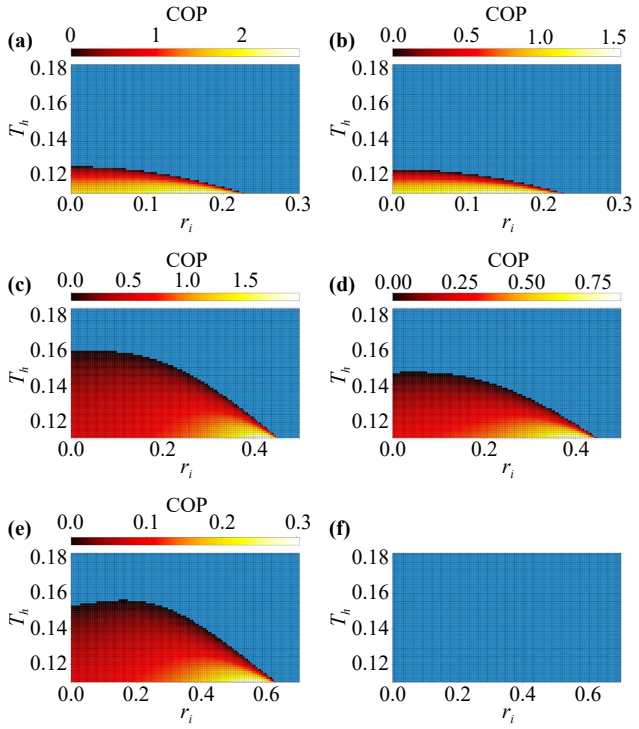

Fig. 9 COP of the refrigerator in the adiabatic case. **(a)** $r^f = 0.3t$ and $\theta = \pi/6$. **(b)** $r^f = 0.3t$ and $\theta = \pi/4$. **(c)** $r^f = 0.5t$ and $\theta = \pi/6$. **(d)** $r^f = 0.5t$ and $\theta = \pi/4$. **(e)** $r^f = 0.7t$ and $\theta = \pi/6$. **(f)** $r^f = 0.7t$ and $\theta = \pi/4$. The color of the color bar corresponds to the COP value, while the blue part indicates the non-refrigerator part. Other parameters are $L = 610$, $k_B = 1$ and $T_c = 0.1t$. The minimum value of T_h is $1.1T_c$.

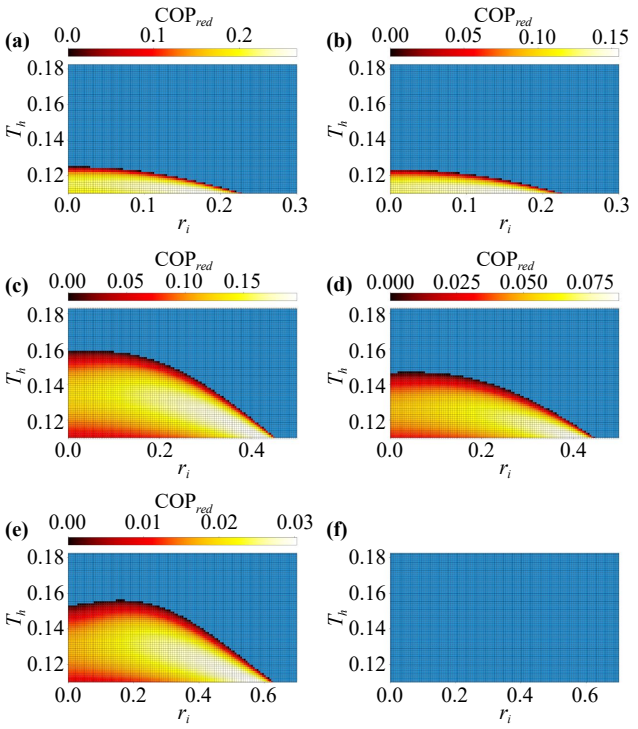

Fig. 10 Reduced COP of the refrigerator in the adiabatic case. **(a)** $r^f = 0.3t$ and $\theta = \pi/6$. **(b)** $r^f = 0.3t$ and $\theta = \pi/4$. **(c)** $r^f = 0.5t$ and $\theta = \pi/6$. **(d)** $r^f = 0.5t$ and $\theta = \pi/4$. **(e)** $r^f = 0.7t$ and $\theta = \pi/6$. **(f)** $r^f = 0.7t$ and $\theta = \pi/4$. The color of the color bar corresponds to the COP_{red} value, while the blue part indicates the non-refrigerator part. Other parameters are $L = 610$, $k_B = 1$ and $T_c = 0.1t$. The minimum value of T_h is $1.1T_c$.

When T_h approaches T_c infinitely, this indicator tends to infinity, but at this point, the refrigerator loses its functional significance in reversibly transporting heat.

Figures 9(a)–(f) present the COP of the refrigerator modes. Similar to the distribution of thermal engine efficiency, high COP mainly occurs when T_h is relatively small. And when r^i and r^f are close, the COP reaches its peak. Unlike the variation of thermal engine efficiency, θ has no significant influence on the variation law of COP. It can be seen that whether $\theta = \pi/6$ or $\theta = \pi/4$, the peak of COP monotonically decreases with the increase of r^f.

To compare COP and COP_C, we introduce the reduced coefficient of performance, i.e, COP_{red}, which is defined as

$$\text{COP}_{\text{red}} = \frac{\text{COP}}{\text{COP}_C}. \tag{8}$$

Taking the same system parameter as those used in Fig. 9, the resulting COP_{red} are shown in Fig. 10. It can be seen that COP_{red} takes relatively large values in the regions with low T_h and moderate r^i. Nevertheless, it is undeniable that the COP of the Otto cycle is somewhat lower than COP_C of the Carnot cycle. However, from the peak evolution trends of COP_{red} and COP, smaller r^f and θ can yield performance comparable to that of the Carnot cycle.

5 Summary

In conclusion, we have investigated the localization and thermodynamic properties of a quasicrystal system featuring simultaneous diagonal and off-diagonal quasiperiodic modulations. We demonstrate that extended, critical, and localized phases can be distinguished not only through the fractal dimension of wave functions but also via quantum phase-space methods, including the Wigner distribution and Wigner entropy. Notably, the Wigner entropy is largest in the critical phase, intermediate in the extended phase, and smallest in the localized phase, offering new insights into localization phenomena in quasiperiodic and disordered systems. Employing this quasicrystal as the working medium in a quantum non-adiabatic cycle, we confirm that the extended phase enables a quantum heat engine mode, while the localized phase supports a heater mode. Surprisingly, through introducing the adiabatic process and constructing a quantum Otto heat cycle, we uncover a fourth operational

mode in this system: a quantum refrigerator mode. In addition, we have made detailed analyses on the efficiency of heat engines and the coefficient of performance of refrigerators. From the results, the efficiency of the heat engine and the performance of the refrigerator still show a certain gap relative to the Carnot cycle, and the high-efficiency regime is mainly concentrated in the region of small T_h. In future work, we will strive to explore optimized cycle mechanisms, such as using different working mediums and rate-controllable cycle process, to further improve the heat engine efficiency and cooling performance, as well as to broaden the high-efficiency operating regime. These results will contribute to the development and utilization of quasiperiodic systems in thermodynamics.

Declarations The authors declare that they have no competing interests and there are no conflicts.

Acknowledgements This research was supported by the Zhejiang Provincial Natural Science Foundation of China under Grant No. LQN25A040012, the start-up fund from Xingzhi College, Zhejiang Normal University, and the National Natural Science Foundation of China under Grant No. 12174346.

References

1. P. W. Anderson, Absence of diffusion in certain random lattices, *Phys. Rev.* 109(5), 1492 (1958)
2. S. Aubry and G. André, Analyticity breaking and Anderson localization in incommensurate lattices, *Ann. Isr. Phys. Soc.* 3, 133 (1980)
3. E. Abrahams, P. W. Anderson, D. C. Licciardello, and T. V. Ramakrishnan, Scaling theory of localization: Absence of quantum diffusion in two dimensions, *Phys. Rev. Lett.* 42(10), 673 (1979)
4. N. Mott, The mobility edge since 1967, *J. Phys. C Solid State Phys.* 20(21), 3075 (1987)
5. F. Evers and A. D. Mirlin, Mirlin, Anderson transitions, *Rev. Mod. Phys.* 80(4), 1355 (2008)
6. L. Sanchez-Palencia, D. Clément, P. Lugan, P. Bouyer, G. V. Shlyapnikov, and A. Aspect, Anderson localization of expanding Bose-Einstein condensates in random potentials, *Phys. Rev. Lett.* 98(21), 210401 (2007)
7. G. Roati, C. D'Errico, L. Fallani, M. Fattori, C. Fort, M. Zaccanti, G. Modugno, M. Modugno, and M. Inguscio, Anderson localization of a non-interacting Bose-Einstein condensate, *Nature* 453(7197), 895 (2008)
8. J. Billy, V. Josse, Z. Zuo, A. Bernard, B. Hambrecht, P. Lugan, D. Clément, L. Sanchez-Palencia, P. Bouyer, and A. Aspect, Direct observation of Anderson localization of matter waves in a controlled disorder, *Nature* 453(7197), 891 (2008)
9. S. S. Kondov, W. R. McGehee, J. J. Zirbel, and B. DeMarco, Three-dimensional Anderson localization of ultra-cold matter, *Science* 334(6052), 66 (2011)
10. F. Jendrzejewski, A. Bernard, K. Müller, P. Cheinet, V. Josse, M. Piraud, L. Pezzé, L. Sanchez-Palencia, A. Aspect, and P. Bouyer, Three-dimensional localization of ultracold atoms in an optical disordered potential, *Nat. Phys.* 8(5), 398 (2012)
11. G. Semeghini, M. Landini, P. Castilho, S. Roy, G. Spagnolli, A. Trenkwalder, M. Fattori, M. Inguscio, and G. Modugno, Measurement of the mobility edge for 3d Anderson localization, *Nat. Phys.* 11(7), 554 (2015)
12. D. Delande and G. Orso, Mobility edge for cold atoms in laser speckle potentials, *Phys. Rev. Lett.* 113(6), 060601 (2014)
13. L. Sanchez-Palencia, Ultracold gases: At the edge of mobility, *Nat. Phys.* 11(7), 525 (2015)
14. H. P. Lüschen, S. Scherg, T. Kohlert, M. Schreiber, P. Bordia, X. Li, S. Das Sarma, and I. Bloch, Single particle mobility edge in a one-dimensional quasiperiodic optical lattice, *Phys. Rev. Lett.* 120(16), 160404 (2018)
15. F. Alex An, K. Padavic, E. J. Meier, S. Hegde, S. Ganeshan, J. H. Pixley, S. Vishveshwara, and B. Gadway, Interactions and mobility edges: Observing the generalized Aubry–André model, *Phys. Rev. Lett.* 126, 040603 (2021)
16. T. Xiao, D. Xie, Z. Dong, T. Chen, W. Yi, and B. Yan, Observation of topological phase with critical localization in a quasi-periodic lattice, *Sci. Bull. (Beijing)* 66(21), 2175 (2021)
17. D. S. Wiersma, P. Bartolini, A. Lagendijk, and R. Righini, Localization of light in a disordered medium, *Nature* 390(6661), 671 (1997)
18. T. Schwartz, G. Bartal, S. Fishman, and M. Segev, Transport and Anderson localization in disordered two-dimensional photonic lattices, *Nature* 446(7131), 52 (2007)
19. Y. Lahini, A. Avidan, F. Pozzi, M. Sorel, R. Morandotti, D. N. Christodoulides, and Y. Silberberg, Anderson localization and nonlinearity in one-dimensional disordered photonic lattices, *Phys. Rev. Lett.* 100(1), 013906 (2008)
20. D. S. Wiersma, Disordered photonics, *Nat. Photonics* 7(3), 188 (2013)
21. M. Segev, Y. Silberberg, and D. N. Christodoulides, Anderson localization of light, *Nat. Photonics* 7(3), 197 (2013)
22. H. E. Kondakci, A. F. Abouraddy, and B. E. A. Saleh, A photonic thermalization gap in disordered lattices, *Nat. Phys.* 11(11), 930 (2015)
23. S. Yu, C. W. Qiu, Y. Chong, S. Torquato, and N. Park, Engineered disorder in photonics, *Nat. Rev. Mater.* 6(3), 226 (2020)
24. Y. J. Chang, J. H. Zhang, Y. H. Lu, Y. Y. Yang, F. Mei, J. Ma, S. Jia, and X. M. Jin, Observation of photonic mobility edge phases, *Phys. Rev. Lett.* 134(5), 053601 (2025)
25. X. Deng, S. Ray, S. Sinha, G. V. Shlyapnikov, and L. Santos, One-dimensional quasicrystals with power-law hopping, *Phys. Rev. Lett.* 123(2), 025301 (2019)
26. N. Roy and A. Sharma, Fraction of delocalized eigenstates in the long-range Aubry–André–Harper model, *Phys. Rev. B* 103(7), 075124 (2021)
27. J. Biddle, D. J. Priour, B. Wang, and S. Das Sarma, Localization in one-dimensional lattices with non-nearest neighbor hopping: Generalized Anderson and Aubry-André models, *Phys. Rev. B* 83(7), 075105 (2011)

28. M. Saha, S. K. Maiti, and A. Purkayastha, Anomalous transport through algebraically localized states in one dimension, *Phys. Rev. B* 100(17), 174201 (2019)
29. L. Z. Tang, G. Q. Zhang, L. F. Zhang, and D. W. Zhang, Localization and topological transitions in non-Hermitian quasiperiodic lattices, *Phys. Rev. A* 103(3), 033325 (2021)
30. B. Hetényi and I. Balogh, Numerical study of the localization transition of Aubry–André type models, *Phys. Rev. B* 112(14), 144203 (2025)
31. H. Yao, H. Khoudli, L. Bresque, and L. Sanchez-Palencia, Critical behavior and fractality in shallow one-dimensional quasiperiodic potentials, *Phys. Rev. Lett.* 123(7), 070405 (2019)
32. S. Das Sarma, S. He, and X. C. Xie, Mobility edge in a model one-dimensional potential, *Phys. Rev. Lett.* 61(18), 2144 (1988)
33. S. Ganeshan, J. H. Pixley, and S. Das Sarma, Nearest neighbor tight binding models with an exact mobility edge in one dimension, *Phys. Rev. Lett.* 114(14), 146601 (2015)
34. T. Liu and H. Guo, Mobility edges in off-diagonal disordered tight-binding models, *Phys. Rev. B* 98(10), 104201 (2018)
35. Y. Wang, X. Xia, L. Zhang, H. Yao, S. Chen, J. You, Q. Zhou, and X. J. Liu, One dimensional quasiperiodic mosaic lattice with exact mobility edges, *Phys. Rev. Lett.* 125(19), 196604 (2020)
36. T. Liu, X. Xia, S. Longhi, and L. Sanchez-Palencia, Anomalous mobility edges in one-dimensional quasiperiodic models, *SciPost Phys.* 12, 027 (2022)
37. X. C. Zhou, Y. Wang, T. F. J. Poon, Q. Zhou, and X. J. Liu, Exact new mobility edges between critical and localized states, *Phys. Rev. Lett.* 131(17), 176401 (2023)
38. T. Liu, H. Guo, Y. Pu, and S. Longhi, Generalized Aubry–André self-duality and mobility edges in non-Hermitian quasiperiodic lattices, *Phys. Rev. B* 102(2), 024205 (2020)
39. Y. Liu, Y. Wang, X. J. Liu, Q. Zhou, and S. Chen, Exact mobility edges, pt-symmetry breaking and skin effect in one-dimensional non-Hermitian quasicrystals, *Phys. Rev. B* 103(1), 014203 (2021)
40. M. Gonçalves, B. Amorim, E. V. Castro, and P. Ribeiro, Critical phase dualities in 1D exactly solvable quasiperiodic models, *Phys. Rev. Lett.* 131(18), 186303 (2023)
41. M. Gonçalves, B. Amorim, F. Riche, E. V. Castro, and P. Ribeiro, Incommensurability enabled quasi-fractal order in 1D narrow-band moiré systems, *Nat. Phys.* 20(12), 1933 (2024)
42. V. K. Varma, S. Pilati, and V. E. Kravtsov, Conduction in quasiperiodic and quasirandom lattices: Fibonacci, Riemann, and Anderson models, *Phys. Rev. B* 94(21), 214204 (2016)
43. H. T. Hu, X. Lin, A. M. Guo, G. Guo, Z. Lin, and M. Gong, Hidden self duality and exact mobility edges in quasiperiodic network models, *Phys. Rev. Lett.* 134(24), 246301 (2025)
44. S. Z. Li, Y.C. Zhang, Y. Wang, S. Zhang, S.L. Zhu, and Z. Li, Multifractal-enriched mobility edges and emergent quantum phases in Rydberg atomic arrays, arXiv: 2501.07866 (2025)
45. X. C. Zhou, B. C. Yao, Y. Wang, Y. Wang, Y. Wei, Q. Zhou, and X. J. Liu, The fundamental localization phases in quasiperiodic systems: A unified framework and exact results, arXiv: 2503.24380 (2025)
46. E. Wigner, On the quantum correction for thermodynamic equilibrium, *Phys. Rev.* 40(5), 749 (1932)
47. M. Hillery, R. F. O'Connell, M. O. Scully, and E. P. Wigner, Distribution functions in physics: Fundamentals, *Phys. Rep.* 106(3), 121 (1984)
48. A. Kenfack and K. Yczkowski, Negativity of the Wigner function as an indicator of non-classicality, *J. Opt. B* 6(10), 396 (2004)
49. A. Banerji, R. P. Singh, and A. Bandyopadhyay, Entanglement measure using Wigner function: Case of generalized vortex state formed by multiphoton subtraction, *Opt. Commun.* 330, 85 (2014)
50. R. Simon, Peres-Horodecki separability criterion for continuous variable systems, *Phys. Rev. Lett.* 84(12), 2726 (2000)
51. R. Taghiabadi, S. J. Akhtarshenas, and M. Sarbishaei, Revealing quantum correlation by negativity of the Wigner function, *Quantum Inform. Process.* 15(5), 1999 (2016)
52. F. Siyouri, M. El Baz, and Y. Hassouni, The negativity of Wigner function as a measure of quantum correlations, *Quantum Inform. Process.* 15(10), 4237 (2016)
53. F. Lu, A. Zhou, S. Cheng, and G. Xianlong, Wigner distribution, Wigner entropy, and anomalous transport of a generalized Aubry–André model, *Phys. Rev. B* 112(17), 174206 (2025)
54. Z. V. Herstraeten and N. J. Cerf, Quantum Wigner entropy, *Phys. Rev. A* 104(4), 042211 (2021)
55. V. Balachandran, S. R. Clark, J. Goold, and D. Poletti, Energy current rectification and mobility edges, *Phys. Rev. Lett.* 123(2), 020603 (2019)
56. M. Saha and S. K. Maiti, Particle current rectification in a quasi-periodic double-stranded ladder, *J. Phys. D Appl. Phys.* 52(46), 465304 (2019)
57. M. Saha and S. K. Maiti, High degree of current rectification at nanoscale level, *Physica E* 93, 275 (2017)
58. H. Yin, J. Hu, A. C. Ji, G. Juzeliunas, X. J. Liu, and Q. Sun, Localization driven super-radiant instability, *Phys. Rev. Lett.* 124(11), 113601 (2020)
59. H. G. Xu and S. Cheng, Quantum transport property and thermodynamic applications of one-dimensional off-diagonal quasiperiodic system, *Phys. Rev. B* 112(2), 024204 (2025)
60. J. Biddle and S. Das Sarma, Predicted mobility edges in one-dimensional incommensurate optical lattices: An exactly solvable model of Anderson localization, *Phys. Rev. Lett.* 104(7), 070601 (2010)
61. T. Liu, H. Y. Yan, and H. Guo, Fate of topological states and mobility edges in one-dimensional slowly varying incommensurate potentials, *Phys. Rev. B* 96(17), 174207 (2017)
62. J. Wang, X. J. Liu, G. Xianlong, and H. Hu, Phase diagram of a non-Abelian Aubry–André–Harper model with p-wave superfluidity, *Phys. Rev. B* 93(10), 104504 (2016)
63. T. Liu, P. Wang, S. Chen, and G. Xianlong, Phase

diagram of a generalized off-diagonal Aubry–André model with p-wave pairing, *J. Phys. At. Mol. Opt. Phys.* 51(2), 025301 (2018)
64. T. Liu, P. Wang, and X. Gao, Phase diagram of the off-diagonal Aubry–André model, arXiv: 1609.06939 (2016)
65. W. Chen, S. Cheng, J. Lin, R. Asgari, and G. Xianlong, Breakdown of the correspondence between the realcomplex and delocalization-localization transitions in non-Hermitian quasicrystals, *Phys. Rev. B* 106(14), 144208 (2022)
66. L. Buffoni, A. Solfanelli, P. Verrucchi, A. Cuccoli, and M. Campisi, Quantum measurement cooling, *Phys. Rev. Lett.* 122(7), 070603 (2019)
67. A. Solfanelli, M. Falsetti, and M. Campisi, Nonadiabatic single-qubit quantum Otto engine, *Phys. Rev. B* 101(5), 054513 (2020)
68. C. Sayrin, I. Dotsenko, X. Zhou, B. Peaudecerf, T. Rybarczyk, S. Gleyzes, P. Rouchon, M. Mirrahimi, H. Amini, M. Brune, J. M. Raimond, and S. Haroche, Real-time quantum feedback prepares and stabilizes photon number states, *Nature* 477, 73 (2011)
69. R. Vijay, C. Macklin, D. H. Slichter, S. J. Weber, K. W. Murch, R. Naik, A. N. Korotkov, and I. Siddiqi, Stabilizing Rabi oscillations in a superconducting qubit using quantum feedback, *Nature* 490(7418), 77 (2012)
70. J. M. Horowitz, and K. Jacobs, Quantum effects improve the energy efficiency of feedback control, *Phys. Rev. E* 89(4), 042134 (2014)
71. J. Zhang, Y. X. Liu, R. B. Wu, K. Jacobs, and F. Nori, Quantum feedback: Theory, experiments, and applications, *Phys. Rep.* 679, 1 (2017)
72. H. Uys, H. Bassa, P. Du Toit, S. Ghosh, and T. Konrad, Quantum control through measurement feedback, *Phys. Rev. A* 97(6), 060102 (2018)
73. K. Prech, J. Aschwanden, and P. P. Potts, Quantum thermodynamics of continuous feedback control, arXiv: 2505.16615 (2025)